Magnetically induced friction damping based on magnetoactive elastomers - a proof of concept

Svenja Hermann, Pauline Butaud, Rafael Teloli, Jean-François Manceau, Maxime Savary, Gael Chevallier

Magnetically induced friction damping based on magnetoactive elastomers - A proof of concept

Svenja Hermann [1,2], Pauline Butaud [1], Rafael de O. Teloli [1], Jean-François Manceau [1], Maxime Savary [2], Gaël Chevallier [1]

[1] *FEMTO-ST Institute, CNRS/UBFC, 24 chemin de l'Epitaphe, 25000 Besançon, France*

[2] *Moving Magnet Technologies SA, 25000 Besançon, France.*

Corresponding authors: svenja.hermann@femto-st.fr, gael.chevallier@femto-st.fr

Abstract

In this work we present a new concept for friction damping which is based on the permanent magnetization and the flexibility of magnetoactive elastomers (MAE). The concept is called "magnetofriction" and is studied on a sandwich structure in the present work. The assembled structure consists of a MAE core and ferromagnetic skins. Due to the magnetization of the MAE, the skins are attracted to the core and the sandwich is assembled without the need of glue or other means of fixation. The magnetic forces generate the normal loading in the contact interfaces between skins and core while a tangential loading is induced by forced vibrations applied to the sandwich beam. Random and harmonic vibration tests reveal the nonlinear dynamic behavior of the sandwich structure and highlight the damping capacity of magnetofriction. The harmonic balance method is used on a nonlinear dynamic model of the system to identify the parameters related to the resonance frequency and damping ratio. The results obtained from the identification state damping ratios up to 9 % under harmonic excitation, which is remarkable for friction damping. In addition, a Finite Element-based model of the structure is implemented to study the local contact states in the sandwich. Multi-physical simulations are performed to analyze the magnetic and mechanical loading in the contact interface. The local results are used to evaluate the overall contact states in the interfaces which determine the absence or presence of friction damping. The simulations show that the vibration amplitude changes the contact state.

Keywords: friction damping, magnetoactive elastomer (MAE), sandwich structure, backbone identification

1. Introduction

Excessive vibrations in mechanical structures may generate undesired noise or even mechanical failure of components in the long term. Since quiet operation and durability are priority requirements during project design stages, different damping technologies have been developed during the last years. These technologies include passive devices, e.g. viscoelastic dampers, or active devices, e.g. piezoelectric actuators coupled with a control circuit. From an energetic point of view, passive devices have advantages over active devices, since they do not require an external power supply. In this work we present an original passive concept for vibration damping based on friction in an assembled structure which contains magnetoactive elastomers.

Magnetoactive elastomers are viscoelastic materials and thus capable to dissipate vibrations into heat efficiently. The viscoelastic damping is independent from the vibration magnitude and is therefore classified as a linear mechanism. However, the main drawback of viscoelastic materials is their sensitivity to temperature and frequency variations [1]. Until today, magnetoactive elastomers have been studied exclusively in the context of the adaptive vibration control by external magnetic fields [2, 3, 4, 5, 6, 7].

Friction is one of the main sources of damping in assembled structures. It is induced by relative motion between mechanically linked components. In the contact interface of the joints, the normal stress distribution is governed by the tightening load [8]. The shear stress field is induced by the vibration loading. Depending on the ratio between normal stress and tangential stress, the contact state can range from total stick to partial sliding to mainly sliding [9]. When partial sliding occurs in the contact interfaces, the vibration energy is dissipated by friction [9, 10]. The dissipation behavior is strongly nonlinear as it is linked to the threshold between the three contact states. The advantages of friction damping are the independence from the excitation frequency and the low dependence on temperature variations.

The design of structures that benefit from frictional dissipation remains challenging due to the nonlinearity. Depending on the system, a variation of the

normal stress, also called contact pressure, can lead to a change of the modal stiffness [11] or the modal mass [12]. Brake [13] and Teloli et al. [14] observed that a decrease of the normal tightening load in structures that are assembled by bolted joints results in a higher frictional damping and also in softening effects (decrease of the contact stiffness) in vicinity of resonance frequencies. In addition, the contact pressure distribution is influenced by geometric irregularities on the macroscopic scale (e.g. uneven or wavy surfaces) and on the microscopic scale (roughness) [15, 16]. An interesting possibility to establish a constant contact pressure is the use of magnetically induced forces. Attractive forces between permanent magnets [17] or between permanent magnets and ferromagnetic materials [18] have been used to establish the contact in joints of vibrating systems in the context of seismic damping. In the recent works of Amjadian et al. [19, 20] the contact pressure is generated by repulsive forces between two permanent magnets. The force is transmitted to a friction pad and its intensity is controlled by the distance between the magnets.

In this work we present a new concept for friction damping in assembled structures. It is based on the use of permanently magnetized elastomer composites, also known as magnetically Hard MagnetoActive Elastomers (H-MAEs) [21]. H-MAEs are composed of magnetic particles and a viscoelastic matrix. Their magnetic behavior is comparable to the behavior of permanent magnets [21]. Their elastic modulus, however, is much lower (order of magnitude: 2 MPa to 10 MPa). The key idea of the concept is to use the permanent magnetization and the high flexibility of H-MAEs in the joints of an assembled structure to obtain an evenly distributed contact pressure that favors energy dissipation by friction. In the present study, the H-MAE is used in the core of a sandwich structure with ferromagnetic skins. The mechanical link is established by the magnetic forces.

The use of flexible magnets instead of stiff magnets is favorable for friction damping as the H-MAE can adapt its shape to the deformation of the skins. The contact is thus maintained even for a relatively high deformation of the structure and the assembly is less sensitive to geometric irregularities. The H-MAE is also less heavy than a permanent magnet with comparable volume. In addition, our concept offers the possibility to combine friction damping with viscoelastic damping.

In order to assess the vibration performances, a so-called Magnetofriction Sandwich Structure (MSS) is subjected to random vibrations and harmonic vibrations around the three first natural frequencies with different excitation amplitudes. The equivalent modal parameters of the test structure are evaluated with an original identification method and reveal a nonlinear behavior of the structure. A numerical model of the experiment is used to show the influence of the excitation amplitude on the local contact state between the core and the skins.

The paper is organized as follows: section 2 presents the concept of magnetically induced friction damping and describes the assembly of the experimental test sample. Section 3 contains the description of the test setup and details the experimental investigations and results. Section 4 contains a numerical study of the local contact parameters that are not accessible in the experiment. The last section consists of conclusions on magnetically induced friction damping and opens perspectives for future studies.

2. Magnetofriction in viscoelastic joints

At the beginning of this section, the concept that allows the combination of friction damping and viscoelastic damping is introduced. The experimental test sample which is used to proof the concept is presented subsequently.

2.1. Concept

The new concept is based on magnetically Hard MagnetoActive Elastomers (H-MAEs) which are used as core of a sandwich structure where they establish the mechanical linkage of the assembly. Fig. 1 illustrates the use of the H-MAE to achieve friction damping in sandwich structures. Fig. 1 (a) sketches an oscillating sandwich beam structure. It is composed of a magnetized H-MAE core which is enclosed by two ferromagnetic skins. The magnetic flux, generated by the magnetized H-MAE, propagates into the magnetically permeable skins (Fig. 1 (b)). The ferromagnetic skins are attracted by the magnetized H-MAE and the magneto-mechanical interactions maintain the skins clamped to the core without additional means of fixation (Fig. 1 (c)). The contact pressure is hence established by the magnetization. When the structure is subjected to transverse vibrations, the sandwich structure is deformed and shear stresses arise in the contact interfaces (Fig. 1 (d)). Normal and shear stresses are now present in the contact area. Their ratio

determines the presence and the magnitude of sliding and therefore of friction damping.

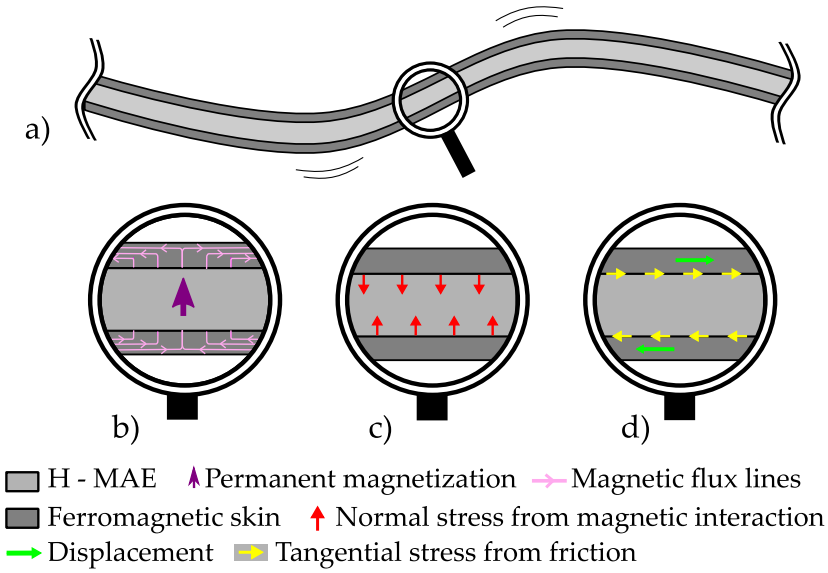

Figure 1: Notational diagram of a part of an oscillating sandwich beam structure (a) and a zoom on one part of the structure sketching the magnetic state (b), the clamping force (c) and the contact situation (d) in the beam.

For small vibration amplitudes, the normal stresses prevail and the contact is maintained without sliding in the interface. In this case, the vibration damping is due to the viscoelasticity of the H-MAE composite. With an increasing vibration amplitude, the tangential stresses increase. Throughout the contact area, more and more parts begin to slide and friction damping occurs. The damping is maximized for a specific ratio of sticking and sliding which is determined by the vibration amplitude. By further increasing the amplitude, the tangential forces become predominant until the contact surfaces mainly slide. In this case, the friction damping is less effective [22, 23]. The concept is called magnetofriction, since contact pressure is established magnetically.

2.2. Test sample

The concept is proven experimentally with the test sample sketched in Fig. 2 (a). The assembly is called Magnetofriction Sandwich Structure (MSS) in the following. It comprises H-MAE patches, steel skins and an aluminum spacer.

The H-MAE is composed of a two-part silicone elastomer MED-4014, provided by NuSil^{TM}, and of magnetically hard NdFeB particles (MQFP-14-12 from Magnequench^{TM}). Details about the elaboration process can be found in [21]. The H-MAE in the present study has a volume fraction of 36 % of NdFeB particles and shows a residual flux density of 0.3 T. The patches used in this study are magnetized in their direction of thickness. The two skins of the MSS consist of the steel alloy M400-50A which is ferromagnetic and magnetically soft. The magnetization curve of the material can be found in the Appendix D (Fig. D.1). The varying width of the sandwich minimizes the effects of the clamp on the experimental results in terms of damping and stiffness. The wider part has three drill holes of which two are used for the alignment of the sandwich in the clamping. The third drill hole is not used in the present study.

The MSS is assembled such as an aluminum spacer and the H-MAE patches form the core between the steel skins. A sample holder is used to ensure the alignment of the components during the assembly. The aluminum spacer is placed in the region of the MSS that is clamped in the experimental setup (Fig. 2 (c)). The stiffness of the spacer makes the clamping less sensitive to the clamping force. The spacer does not contribute to the generation of the contact pressure as it is magnetically neutral. The spacer is maintained in place by the clamping force that fixes the MSS in the experimental setup. The H-MAE core is positioned adjacent to the spacer in the narrow part of the sandwich. The core does not consist of one continuous H-MAE layer since the size of the magnetization chamber limits the patch size. The upper part of the core is therefore composed of five magnetized H-MAE patches. They are oriented such as the magnetization of two adjacent patches is opposed (Fig. 2 (b)). It is impossible to position patches with the same direction of magnetization next to each other in the MSS since their outer regions repel each other due to the magnetic forces in this configuration.

In the narrow part of the sandwich, the magnetic forces between the H-MAE patches and the metal sheets maintain the structure assembled. No glue or bolts are necessary for the assembly and the structural integrity. To highlight the benefits of the magnetic forces compared to more classical adhesion forces, the structure has also been tested in a configuration where the patches were partly glued. A glue point has been applied to the center of each patch on each side that is in contact with the skin. The amount

of glue remained small and it was not applied on the entire patch surface (Appendix F, Fig. F.1). This approach was chosen on the basis of additional experiments that revealed an accumulation of the glue in the intersections between H-MAE patches. The glued configuration is called gMSS.

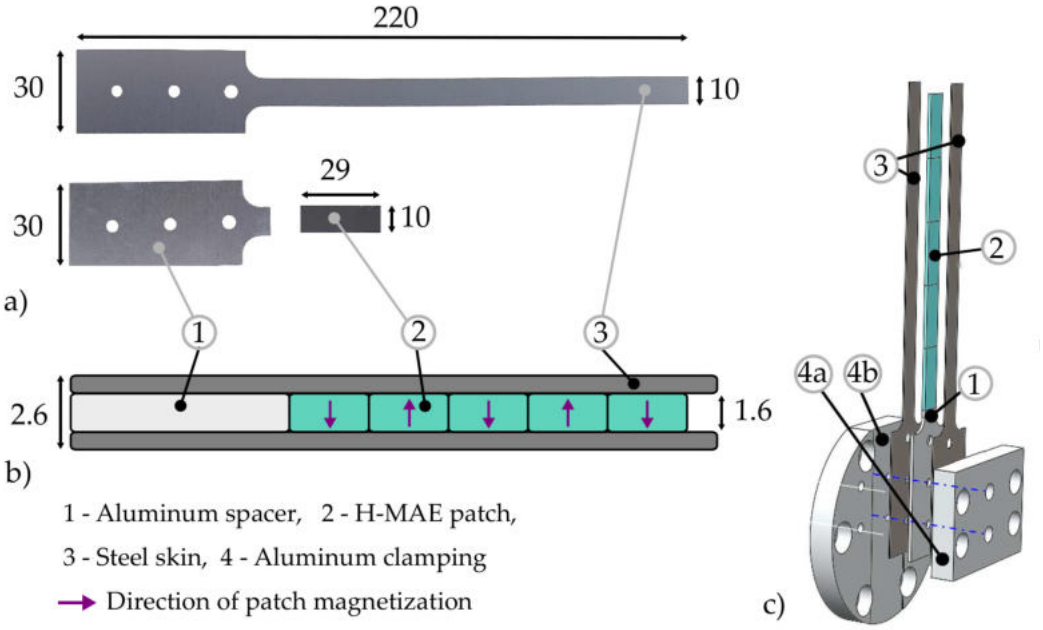

Figure 2: Components of the MSS (a), schematic side view of the assembled MSS (b) and schematic view of the clamping (exploded view) (c).

3. Vibration experiments

In this section, the experimental investigations on magnetically induced friction damping are presented. The experimental setup is explained at the beginning of the section. Afterwards, the random and harmonic excitation methods, which are used to characterize the dynamic behavior of the sandwich structure, are detailed. The two different excitation strategies are illustrated by the experimental results and first conclusions on the dynamic behavior are drawn. In the subsequent section, the identification of the modal parameters for the two different excitation methods is presented.

3.1. Experimental setup

In the experimental setup, the sandwich structure is clamped to an electromagnetic shaker (Tira TV 52125 200 N) as shown in Fig. 3 (a). The necessary power for the shaker is delivered by an amplifier. A triaxial B&K DeltaTron® accelerometer (Type 4520) is glued to the clamp to drive the base-excitation tests. The acceleration component $\boldsymbol{a}_2(t)$ measured in direction e_2 is used as reference signal in the post-processing. The structure velocity is measured with a contactless Polytec vibrometer PSV-500 Xtra®. The velocity measurements are either performed on a single point with the position (x_1, x_3) on the MSS or on multiple points. In the second case, a velocity field $\boldsymbol{v}_2(x_1, x_3, t)$ is obtained in direction e_2. For the random excitation tests, the data acquisition and the post-processing are performed by the software of the laser vibrometer (Fig. 3 (b)). During the harmonic oscillation, the excitation amplitude is feedback-controlled by in-house subroutines [14]. The algorithms are implemented in Matlab® and transmitted via a NI9234 hardware.

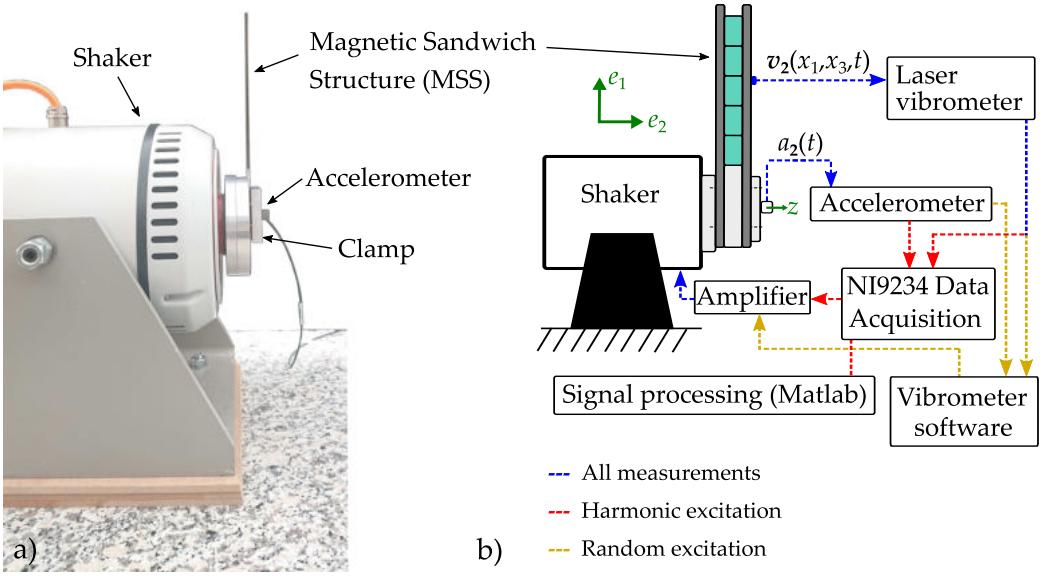

Figure 3: Experimental setup with MSS specimen mounted on the electromagnetic shaker in side view: photograph (a) and schematic view (b).

3.2. Random excitation

The first part of the experiment consists of random vibration tests with the MSS and the gMSS. The goals of these tests are the identification of the first three vibration modes and the identification of the extended modal parameters, natural frequency f_0 and damping ξ, that depends on the vibration amplitude. The frequencies of the modes are used to define the frequency ranges for the harmonic excitation tests and the modal parameters are used to compare the MSS with the gMSS. The two different RMS acceleration levels $0.1\,\mathrm{m/s^2}$ and $1\,\mathrm{m/s^2}$ are used for the excitation. The structures are subjected to random vibrations in a frequency range between 20 Hz and 370 Hz. During each test, single-point measurements of the velocity are performed on one point which is represented in the schematic view of Fig. 4 (a). The frequency response functions (FRFs) are estimated for each frequency f on the measurement points using the H_1 estimator (Eq. (1)). The estimator is calculated from the average autopower $\overline{S}_{aa}$ of the input signals $\hat{a}(f)$ (acceleration) and the average crosspower $\overline{S}_{av}$ of the same input signals and the output signals $\hat{v}(f)$ (velocity) obtained from n repetitions of the measurement, yielding:

$$H_1(f) = \frac{\overline{S}_{av}(f)}{\overline{S}_{aa}(f)} = \frac{\frac{1}{n}\sum_{j=1}^{n} \hat{a}_j(f)\hat{v}_j^H(f)}{\frac{1}{n}\sum_{j=1}^{n} \hat{a}_j(f)\hat{a}_j^H(f)}\,, \tag{1}$$

where $(\bullet)^H$ denotes the complex conjugate transpose.
The FRFs have been estimated for each of the four random excitation tests. The result of the MSS for the high excitation level is shown in Fig. 4 (b) as an example. The first three resonances are located in the measurement range and are well separated.

3.3. Harmonic excitation

In the second part of the experiment, the MSS is subjected to harmonic vibrations with different acceleration magnitudes. The goal of this study is to highlight the nonlinear behavior of the structure with respect to the excitation amplitude experimentally. A controlled step-sine procedure is used for the excitation. During this type of test, the MSS is excited in the steady-state regime with a fixed base-acceleration magnitude, whereas the excitation frequency is incrementally varied around each resonance frequency. Due to the acceleration and frequency control, this procedure is well adapted to identify the nonlinear behavior of vibrating structures. The procedure is described in detail in [14]. In the present study, the three resonance modes of the MSS

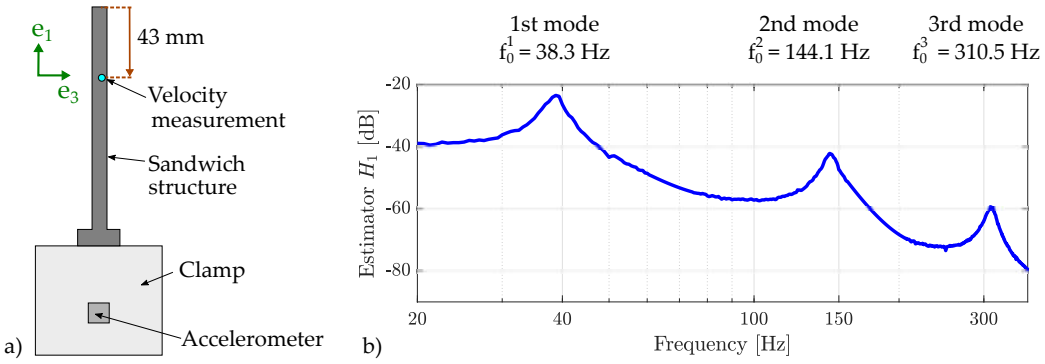

Figure 4: Schematic front view of the clamped MSS (a) and estimation of the FRFs by H_1 (b) for the MSS with an RMS acceleration magnitude of $1\,\mathrm{m/s^2}$.

are characterized for the accelerations and frequencies summarized in Tab. 1. The frequency is varied in steps of $\Delta f = 2\,\mathrm{Hz}$ during the experiments. The measurements are performed increasing and decreasing the excitation frequency to ensure that the evolution of the response in the vicinity of the resonance frequency is well captured.

Resonance mode	Acceleration magnitude [m/s^2]										Frequency range [Hz]
	0.1	0.5	1	2	5	10	20	50	75	90	
1	x	x	x	x	x						10 – 40
2			x	x	x	x	x	x			70 – 150
3			x	x	x	x	x	x	x	x	210 – 320

Table 1: Summary of the acceleration magnitudes $\hat{a}_k$ and frequency range $[f_1 - f_n]$ used the step-sine tests for each resonance mode. x – applied during test

As an example for the step-sine tests, amplitude and phase of the FRFs of the third resonance mode for different acceleration amplitudes are shown in Fig. 5 (a) and Fig. 5 (b), respectively. The amplitude represents the ratio of the velocity measured on the structure and the acceleration measured on the base. The results indicate a nonlinear behavior of the MSS with respect to the excitation amplitude: the resonance frequency decreases as the base acceleration amplitude increases and the shape of the amplitude peaks is modified. Under these excitation conditions, note that the amplitude peaks of the FRFs at the resonance frequencies tend to decrease and incline to the left. The so-called softening-effect takes place in assembled structures due to the presence of partial sliding that is responsible for reducing the contact stiffness.

This nonlinear behavior is related to the friction dissipation [22, 23, 12, 14]. The results shown in Fig. 5 prove the existence of friction in the MSS and hence the concept of magnetofriction. Limiting frequencies for sliding and adhesion have been obtained by numerical modeling of the experiment. The limits are represented in Fig. 5. Two resonance frequencies are not included in the interval due to the fact that the clamping was not exactly represented in the model. However, the experimental and numerical results are in good accordance and a varying contact state is confirmed.

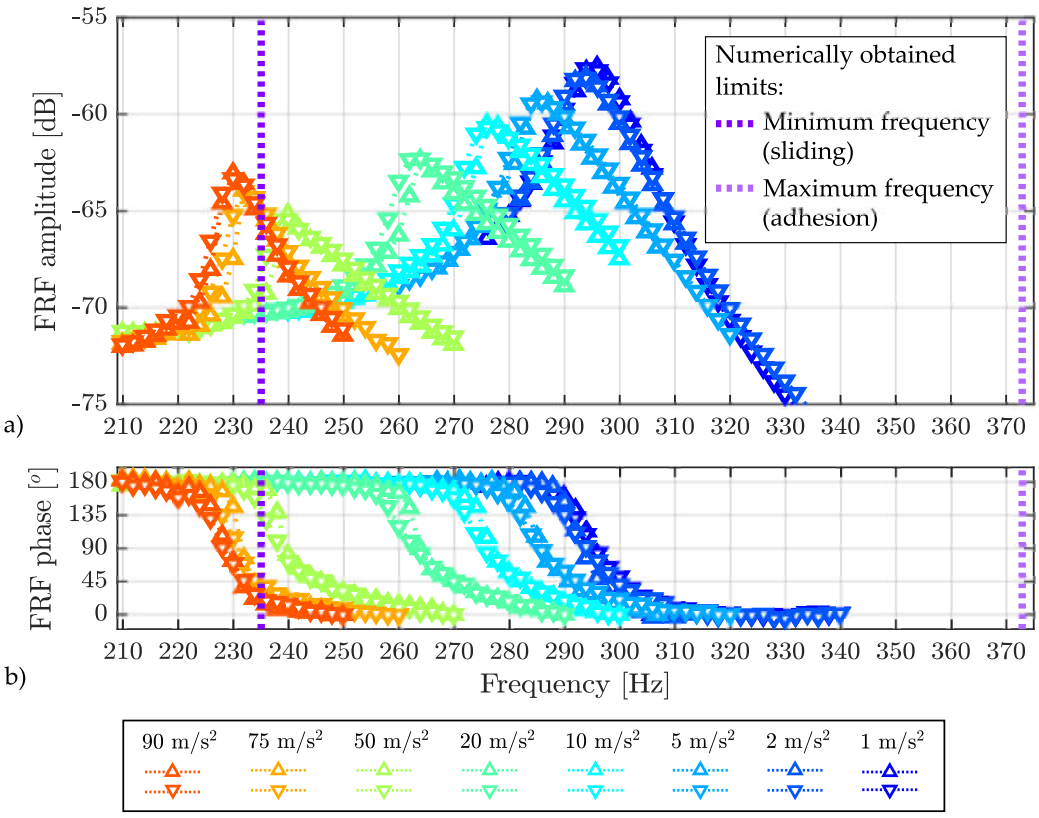

Figure 5: Results of harmonic vibration test: amplitudes and phases of the FRFs obtained for eight different acceleration amplitudes with either increasing -△- or decreasing -▽- frequency during the measurement.

A comparison of the tests with increasing and decreasing frequency reveals jumps in vicinity of the resonances (Fig. 5). In fact, the assembled configuration of the MSS depends on the last sliding between the core and the skins. This sliding occurs around the resonance state, thus the assembled state is

modified slightly during each step-sine test. The effect is present and visible between two tests with the same base-acceleration magnitude and different frequency sweeping directions. The results of the two first vibration modes can be found in the Appendix A (Fig. A.1 and Fig. A.2). The identification of the modal parameters f_0 and ξ of the harmonic excitation tests is presented in the second part of section 3.4.

3.4. Identification of modal parameters

For the random vibration tests, a conventional fitting procedure of the vibrometer software is used to identify the natural frequencies ${f_0}^{(i)}$ and modal damping $\xi^{(i)}$ of the first three modes. The results are summarized in Tab. 2. All natural frequencies of the MSS decrease significantly as the excitation level increases while the natural frequencies of the gMSS decrease slightly. The evolution of ${f_0}^{(i)}$ is related to the stiffness which depends mainly on the slip in the interfaces in our case. Once slip occurs, the stiffness decreases. The resulting decrease in the stiffness of the structure ("softening" effect) is responsible for the shift of ${f_0}^{(i)}$. Sliding is prevented by the glue in the gMSS; conversely, the amount of sliding is higher in the MSS, which is required for friction damping and therefore, the assembly technique based on magnetic forces is more favorable for friction damping than the use of glue. In addition, the glue slightly increases the stiffness of the structure. As a result, the resonance frequencies are higher for the gMSS than for the MSS. The results are less obvious for damping because the effect of stiffness nonlinearity on structures under random excitation is to widen the frequency bandwidth [24]. Damping has the same effect: it is impossible to separate the sources of damping sources, therefore it is difficult to conclude. This is not a problem since the harmonic tests allow us to evaluate the dependence of the damping on the amplitude of the vibration.

Sample	Excitation	1^{st} mode		2^{nd} mode		3^{rd} mode	
	a_{RMS} [m/s^2]	f_0^1 [Hz]	ξ^1 [%]	f_0^2 [Hz]	ξ^2 [%]	f_0^3 [Hz]	ξ^3 [%]
MSS	0.1	40.6	5.5	147.6	3.0	315.1	2.3
	1.0	38.3	6.1	144.1	4.2	310.5	3.1
gMSS	0.1	41.4	6.3	152.6	3.6	332.2	2.9
	1.0	40.8	4.5	152.4	3.4	332.5	3.6

Table 2: Resonance frequencies f_0 of the first three vibration modes obtained for the random excitation with different excitation levels with the MSS the gMSS.

Under harmonic excitation, the experimental results indicate that the stiffness and the damping evolve in a nonlinear manner. Thus, for identifying the equivalent modal parameters, each bending mode of the MSS is modeled based on the following nonlinear differential equation:

$$m^{(i)}\ddot{q}(t) + c^{(i)}\dot{q}(t) + k^{(i)}q(t) + \beta^{(i)}\dot{q}(t)q^2(t) + \alpha^{(i)}q(t)^3 = Ca\sin(\Omega t), \quad (2)$$

where $\Omega = 2\pi f$ corresponds to the angular excitation frequency. The parameters $m^{(i)}$, $c^{(i)}$, $k^{(i)}$ correspond to modal values of mass, damping and stiffness, respectively, of the i^{th} vibrating mode; $\beta^{(i)}$ and $\alpha^{(i)}$ are the modal parameters that govern the nonlinear behavior of the structure. They are related to the nonlinear damping and nonlinear stiffness, respectively. The identification procedure performed to estimate the model parameters is formulated into a harmonic balance framework considering a single harmonic. Further details related to this identification strategy are addressed in [14]. It is important to point out that, in the present case, the acceleration and the velocity have been measured and the excitation force is not known. Thus, the method has been improved to process tests considering a base-acceleration excitation. A preliminary step is to derive the excitation force from the acceleration measured at the base.

Additional full-field measurements show that the mode shape, and hence the modal mass $m^{(i)}$, does not change significantly with the acceleration magnitude (Appendix B, Fig. B.1). Moreover, modal damping is composed of a linear viscous part and a nonlinear viscous one that depends on the square of the displacement. The nonlinear stiffness force is composed of linear part and a cubic contribution. Based on the harmonic balance formulation, the resulting expressions of damping and frequency are given by:

$$f_0^{(i)} = \frac{1}{2\pi}\sqrt{\frac{k^{(i)} + \frac{3}{4}\alpha^{(i)}\mathcal{Q}^2}{m^{(i)}}}, \qquad \xi^{(i)} = \frac{1}{\pi m^{(i)} f_0^{(i)}}\left(c^{(i)} + \frac{\beta^{(i)}\mathcal{Q}^2}{4}\right), \quad (3)$$

where $\mathcal{Q}$ is the fundamental harmonic amplitude of the system response.

Figure 6 depicts the results of the post-processed identification as the dependence of the natural frequency and damping on the vibration amplitude. These graphs are usually presented under the name "backbone" in the literature [25].

The identification process has led to build the backbones corresponding to the first three modes of the structure. As for all the structures that implement a friction-induced damping solution, the natural frequencies of each mode decrease with the vibration amplitude [13]. For this new concept, so-called magneto-friction structures, the dependence is stronger than in most of the cases studied [10, 14, 26]. This reflects the fact that a large amount of strain energy is mobilized in the interface. A Modal Strain Energy Fraction (MSEF) can be defined by analogy with the electro-mechanical coupling [27] or the viscoelastic induced damping criteria [28], which is given by:

$$K^{(i)} = \sqrt{\frac{\max(f_0^{(i)}) - \min(f_0^{(i)})}{\min(f_0^{(i)})}}. \tag{4}$$

From the MSEF point of view, the setup benefits from the fact that the interface is distributed over the entire domain. Concerning the damping, the results are remarkable since more than 8% of damping was obtained on the first mode. Only the assembly studied by [9], the Rubbing Beam Resonator (RuBber) structure, produced better results. In both cases, MSS and RuBber, it is the ability to produce relatively uniform contact pressures that has allowed us to achieve these excellent performances.

Case	MSS	MSS	MSS	ORION	RubBeR	BRB	MAIAS	Piezo-R
Ref	/	/	/	[14]	[9]	[26]	[28]	[29]
Mode	1st	2nd	3rd	6th	1st	7th	4th	1th
K [%]	83	76	55	11	78	20	10	10
ξ [%]	9	5	4	1.2	15	0.4	8	1

Table 3: Bench-marking between several results from the literature. Modal Strain Energy Fraction indicates the involved energy. Modal damping indicates the target performance.

To illustrate how remarkable the performance obtained with the MSS structure is, Table 3 presents a comparison in terms of MSEF and damping between the MSS and other structures described in the literature. The RubBer experiment presents comparable performances, even slightly superior. It uses a very original device to manage the dry friction. But technologically compared to RubBer, the device used by MSS is really much simpler and easier to implement. Brake-ReußBeam (BRB) and ORION are using bolted joints. Their performance is definitely not as good. MAIAS [28] uses viscoelastic joints that allows to get similar performances in terms of damping but with

a lower MSEF. Piezo-R uses a piezoelectric device shunted with a resistance that leads the same result than for a optimized bolted structure like ORION. Thus, this magneto-friction technology appears to be a promising technology for vibration damping.

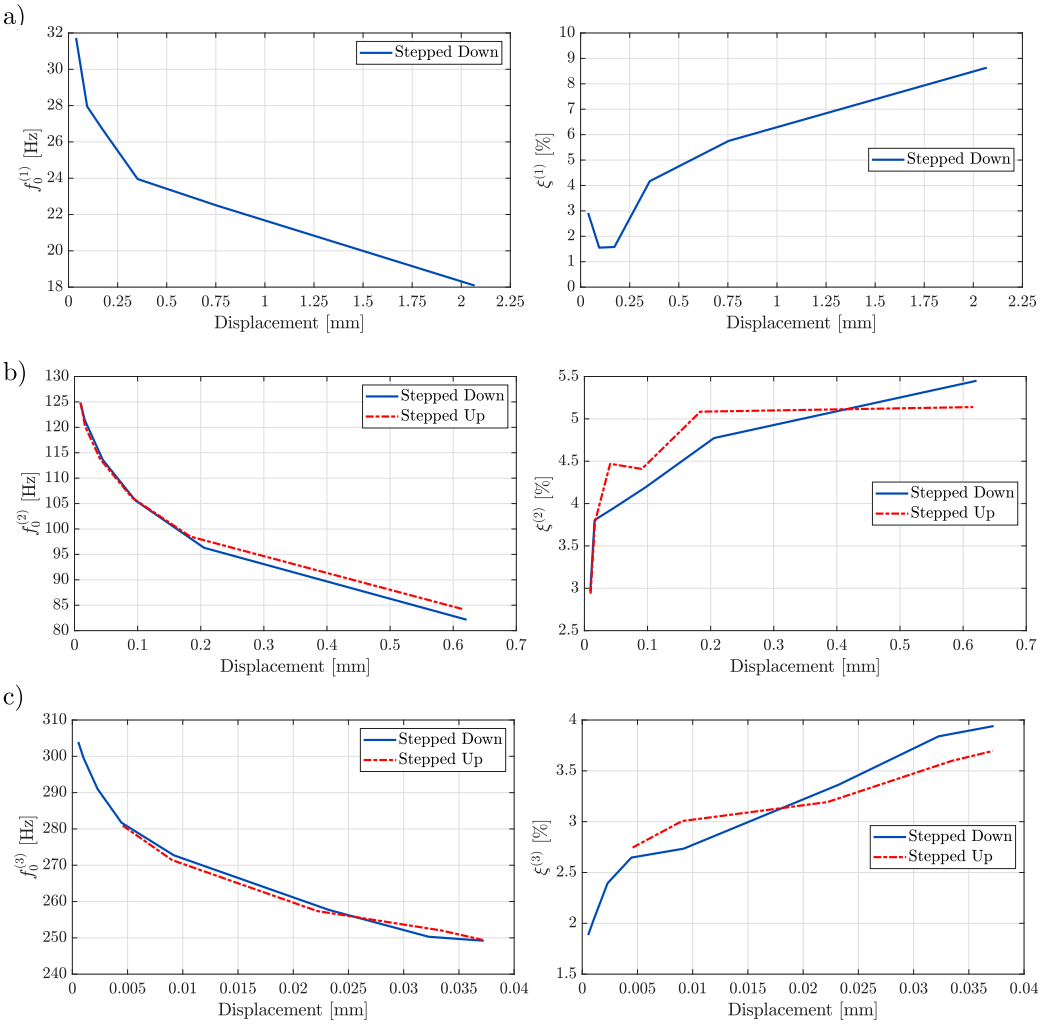

Figure 6: Backbones calculated for the resonance frequency $f^{(i)}$ and the damping $\xi^{(i)}$ for the first three resonance mode of the MSS. The displacement denotes the vibration magnitude.

4. Numerical study of the local contact state

The experimental results show a dependence of the resonance modes on the acceleration amplitude which is characteristic for systems with friction damping ([12, 22, 23]). This type of dissipation is caused by partial sliding in the contact interface at the positions where the shear stress is superior to the normal stress. It is extremely difficult to analyze the local contact state experimentally; hence a numerical model of the sandwich structure is implemented in FE code. The so-called digital twin is used to study the stress contributions that determine the contact state: the magnetically induced normal stress on the one hand and the vibration induced shear stress on the other hand.

4.1. Implementation of the digital twin

In the present study, the digital twin is a two-dimensional representation of the sandwich (Fig. 7). The digital twin has the same geometric and material properties as the experimental sample. The Maxwell stress tensor is commonly used to calculate the magnetic loading. Force calculations based on this tensor can be performed on material interfaces that separate magnetizable and non-magnetizable materials [30]. For this reason, a gap is required between the sandwich core and each of the skins.

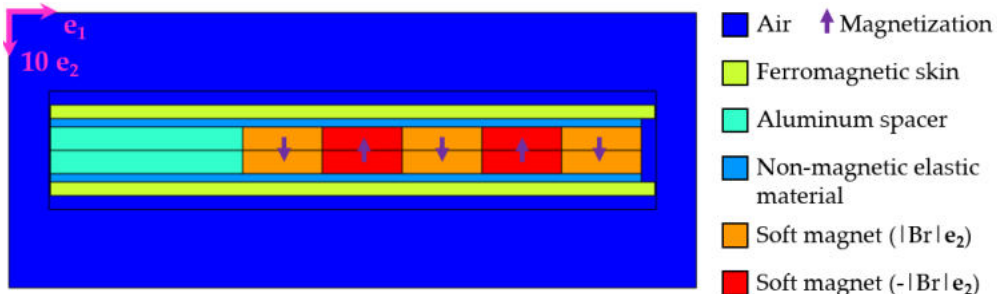

Figure 7: Numerical model of the sandwich structure, axis ratio $\boldsymbol{e}_2$:$\boldsymbol{e}_1$ = 10:1 in graphic representation for better visibility.

The size of the gap set to 0.3 mm. According to the parametric study shown in Appendix E, this value is the best compromise between the calculation time and the accuracy of the local quantities obtained by the FE analysis. To establish the mechanical contact in the sandwich, however, a non-magnetic elastic material is situated in the gaps. The patches are arranged with alternating direction of magnetization in the model similar to the experiment. The

components of the sandwich are meshed with a quadratic mesh (element size 0.1 mm – 0.2 mm). A triangular mesh with an element size between 0.1 mm and 2 mm is used for the air surrounding the sandwich. The mesh is refined in vicinity of the sandwich to increase the accuracy of the local magnetic quantities.

The H-MAE patches are permanently magnetized and the variations of the magnetic field $\boldsymbol{H}$ remain small. Under these conditions, the composite material can be described by the linear magnetic material model shown in Eq. (5). This material model relates the magnetic flux density $\mathbf{B}$ to $\mathbf{H}$ using the magnetic constant μ_0, the magnetic permeability μ_r and the residual flux density $\boldsymbol{B_r}$:

$$\boldsymbol{B} = \mu_0 \mu_r \, \boldsymbol{H} + \boldsymbol{B_r} \; . \tag{5}$$

The nonlinear magnetic behavior of the steel skins is directly implemented as behavior law in the numerical model (cf. Appendix D, Fig. D.1). The magnetically neutral behavior of the aluminum spacer, the surrounding air and the non-magnetic elastic material can also be described by Eq. (5) with $\boldsymbol{B_r} = \mathbf{0}$.

The mechanical strain remains small in the test cases; therefore a linear mechanical behavior of the skins and the core is implemented in the model. In the behavior law, the strain tensor $\boldsymbol{\varepsilon}$ is linked to the stress tensor $\boldsymbol{\sigma}$ by the fourth order stiffness tensor $\boldsymbol{C}$:

$$\boldsymbol{\sigma} = \boldsymbol{C} : \boldsymbol{\varepsilon} \; . \tag{6}$$

The materials are modeled as mechanically isotropic and the corresponding stiffness tensors are hence determined by their Young's moduli E and their Poisson's ratios ν. The material in the gap between the core and the skins possesses the same mechanical properties as the H-MAEs. All magnetic and mechanical material parameters are listed in table 4.

In the numerical simulations, a structural magneto-mechanical coupling is implemented to calculate the magnetic forces between the components of the sandwich. The calculation of the local magnetic fields accounts for the influence of the shape of the different parts of the sandwich on their internal magnetic fields [31]. MAEs are generally known for their magneto-elastic material coupling represented by a dependence of their elastic modulus on externally applied magnetic fields [32] or magnetostriction [33]. The material

Material	μ_r	$\lvert B_r \rvert$	E [MPa]	ν
Air	1.0	-	-	-
Ferromagnetic skin	dependent on H^*	-	210 000	0.30
Aluminum spacer	1.0	-	70 000	0.35
H-MAE	1.1	0.3	10	0.49
Gap	1.0	-	10	0.49

Table 4: Material properties of the different materials modeled in the digital twin. *cf. Appendix D, Fig. D.1

coupling is strong in magnetically soft MAEs when the material is not magnetically saturated [34]. In the present case, however, the material coupling can be neglected for several reasons. The MAE in the present study is magnetically hard and initially magnetized. The magnetization has no significant influence on the elastic modulus of the MAE used in the present study [21]. This behavior is due to the comparatively high stiffness of the elastomer matrix, which has a high influence on the intensity of magneto-elastic couplings in MAE [35]. In addition, no external magnetic field is applied and the variation of the magnetic field in the sandwich remains small during the tests due to the small modal displacements. Furthermore, the magnetized MAE has a low magnetic permeability in the direction of magnetization. This state is comparable to the magnetic saturation regime of magnetically soft MAEs for which the magneto-elastic coupling effect is weaker than prior to the saturation [34]. For these reasons, uncoupled magnetic and the mechanical behavior laws are used to model the MAE material.

4.2. Study cases

Two numerical study cases are performed to determine the magnetically induced normal stress and the shear stress induced by vibrations, respectively. In order to evaluate the stresses, the sliding in the contact interfaces is blocked. For the magnetic part of the simulations, performed in a quasi-static regime, the absence of electric fields and in-plane magnetic fields are assumed. The mechanical part of the simulations assumes in-plane mechanical strains and a stationary regime. The remaining magneto-mechanical governing equations are stated in the Appendix D.

The first study case concerns the magneto-mechanical loading that maintains the sandwich structure assembled. Fully coupled magneto-mechanical sim-

ulations have been performed considering the attraction force between the skins and the H-MAE as the only loading. In the first step, the surface force density of magnetic origin, $\boldsymbol{f}_S^{mag}$, is calculated on the boundaries of the skins and the core. The assumptions regarding the absence of currents and the quasi-static regime allow to calculate the forces by the help of the Maxwell stress tensor $\boldsymbol{T}$ in the non-magnetic materials surrounding the skin and the surface normal $\boldsymbol{n}$ on the boundaries of the magnetic components ([30]):

$$\boldsymbol{f}_S^{mag} = \boldsymbol{T} \cdot \boldsymbol{n} = \left(\frac{1}{\mu_0} \boldsymbol{B} \otimes \boldsymbol{B} - \left(\frac{\boldsymbol{B} \cdot \boldsymbol{B}}{2\mu_0} \right) \boldsymbol{I} \right) \cdot \boldsymbol{n} \, , \tag{7}$$

with $\otimes$, $\cdot$ and $\boldsymbol{I}$ representing the vector product, the scalar product and the identity matrix, respectively. The force density is then applied as mechanical loading on the boundaries of the skins and the core. The resulting normal stress σ_{22} in the contact interface, corresponds to the component of $\boldsymbol{f}_S^{mag}$ in the direction $\boldsymbol{e}_2$:

$$\sigma_{22} = \boldsymbol{f}_S^{mag} \cdot \boldsymbol{e}_2 \, . \tag{8}$$

The load case of the second study is purely mechanical. The third bending mode is chosen for the numerical study in this paper since the full-field velocity was easier to measure for this mode than for the two other ones. The experimental modal velocity field of the third bending mode has been obtained from the multi-point measurements with three different acceleration magnitudes presented in the Appendix B. Based on the experimental results obtained for a base acceleration of $a = 1\,\mathrm{m/s^2}$, a displacement field function compatible with the numerical mesh is generated by interpolation (cf. Appendix D, Fig. D.2). The displacement functions of the two additional vibration amplitudes are obtained by multiplying the displacement function by the corresponding vibration level. This method can be used as mode shapes are similar regardless of the vibration magnitude (cf. Fig. B.1). The displacement fields are applied on the upper skin on the outside of the sandwich, where they have been measured in the experiment, in three different load cases as stationary mechanical loading. During the study, the central line in the spacer is not allowed to move in the $\boldsymbol{e}_1$ direction and the bottom edge of the sandwich is fixed.

4.3. Results of normal and shear stress

The normal stress σ_{22} in the interface between the upper skin and the non-magnetic elastic layer is represented in Fig. 8. The normal stress is mainly

negative which means that the skin is attracted by the H-MAE core. Attraction forces were also obtained for the second skin. In the middle region of the patches and the spacer, the stress magnitude is nearly constant. Stronger variations of the stress are observed in vicinity of geometric or material discontinuities, like corners and material interfaces. The distribution of the normal stress in the interface is directly related to the intensity and the distribution of the magnetic flux density (cf. Eq. (7)). The magnetic flux concentrates near the intersections of magnetic patches where it forms dense closed loops (cf. Appendix E, Fig. E.1). As the stress increases with the magnitude of the flux density, it is higher at an intersection of two patches than in the middle of a patch. Furthermore, the distribution of the magnetic flux generates a low normal stress in the clamping and an increased normal stress at the tip of the sandwich. Even though the contact pressure varies locally, it is well distributed in the contact interface compared to common mechanical assemblies, such as bolted joints (cf. [16] for example). In addition, the pressure has a relatively weak magnitude which is of great technological interest as it offers the possibility to obtain partial sliding (and hence friction damping) at low vibration magnitudes.

The shear stress σ_{12} in the contact interface of interest is shown in Fig. 8 (b) for the three studies with different base acceleration magnitudes. The qualitative evolution of the shear stress in the interface is similar for the three cases since the mechanical loading is generated by one displacement field function with different amplitudes. The shear stress is low near the fixation, where the modal displacements are small and the structure is hence not deformed by the loading. The direction of the shear stress changes at the points where the displacement of the structure is at a local maximum or minimum (cf. Appendix D, Fig. D.2).

4.4. Evaluation of the contact state

A Coulomb friction model (cf. [36] for example) is used to study whether the contact surfaces show a relative movement or not (sliding or sticking). According to the Coulomb friction model, sliding occurs when the ratio of tangential and normal stress are equal to a friction coefficient: $|\sigma_{12}|/|\sigma_{22}| = c_\mu$. In the numerical model, however, the relative movements are blocked. In this case, sliding is represented by a stress ratio of $|\sigma_{12}|/|\sigma_{22}|$ that is equal to

or greater than c_μ:

$$\text{Contact state}: \begin{cases} |\sigma_{12}| < c_\mu |\sigma_{22}| & \rightarrow \text{sticking} \\ |\sigma_{12}| \geq c_\mu |\sigma_{22}| & \rightarrow \text{sliding} \end{cases} \tag{9}$$

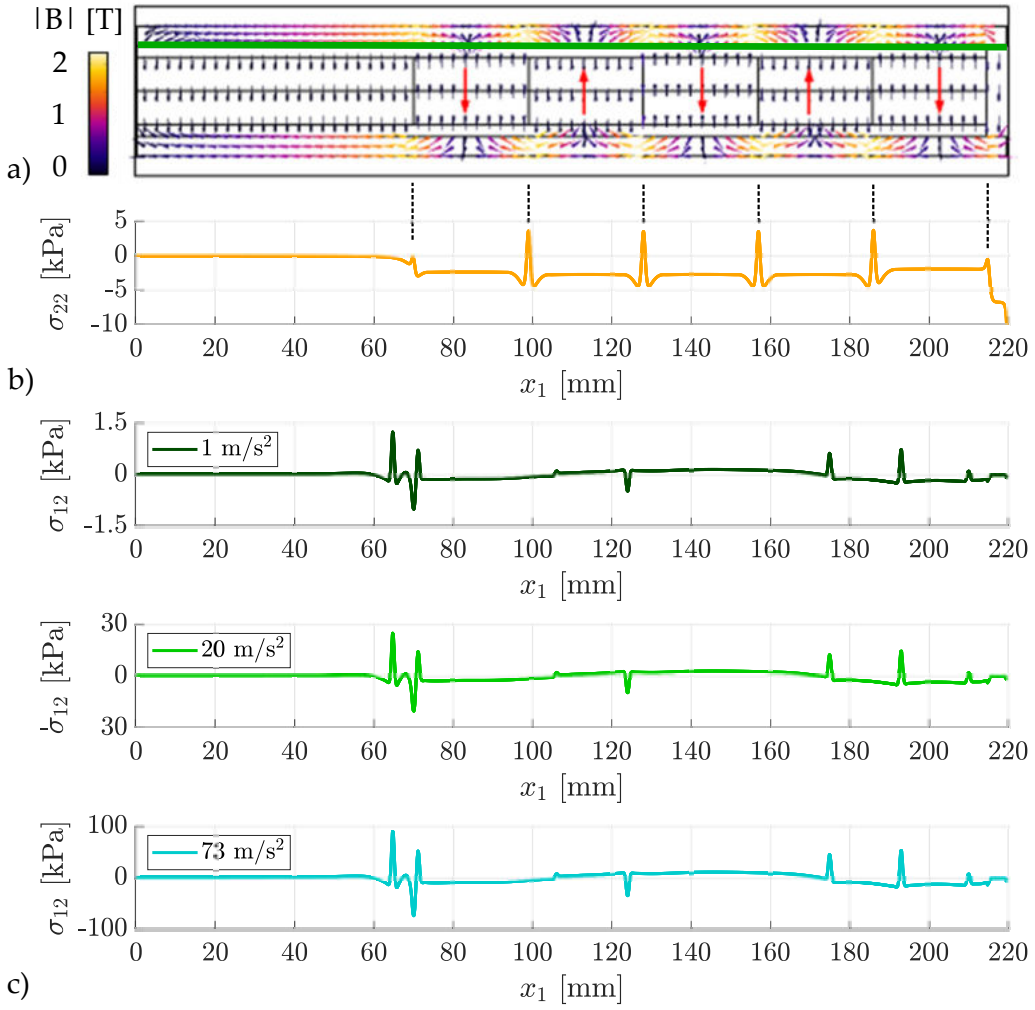

Figure 8: Distribution of the magnetic flux density B, direction of H-MAE magnetization (red arrows) and evaluation interface (green line) in the model (a), magnetically induced normal stress σ_{22} (b) and mechanically induced shear stresses for the three tested excitation magnitudes (c) in the evaluation interface.

To analyze the contact state, the stress ratio $|\sigma_{12}|/|\sigma_{22}|$ is determined for the three acceleration magnitudes. The result is shown in Fig. 9. In one of our studies on the friction behavior of the H-MAE, a friction coefficient of 1 has been measured experimentally. The value is highlighted in Fig. 9 by a red line and will be used to evaluate the contact state in the following.

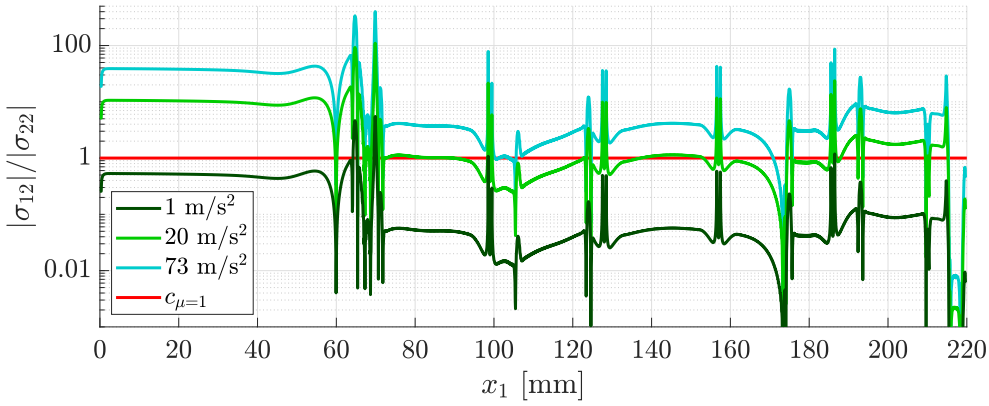

Figure 9: Distribution of the stress magnitude ratio $|\sigma_{12}|/|\sigma_{22}|$ for different acceleration amplitudes and the friction coefficient $c_\mu = 1$ in the evaluation interface of the sandwich structure.

For the lowest excitation magnitude of $1\,\mathrm{m/s^2}$, the main part of the curve lies below c_μ, thus the contact surfaces are mainly sticking together. For the intermediate excitation magnitude of $20\,\mathrm{m/s^2}$, the ratio $|\sigma_{12}|/|\sigma_{22}|$ is of the same order of magnitude as c_μ. Parts of the contact surfaces are sticking while others are sliding. Friction damping occurs principally for this contact state. For the highest excitation magnitude of $73\,\mathrm{m/s^2}$, the main part of the curve lies above c_μ which means that there is mainly sliding in the contact interface.

The combination of experimental results, numerical simulations and the friction model allows to study the evolution of the contact in the digital twin of the sandwich structure. Since the concept of H-MAE based friction damping is fairly new, the model comprises several assumptions in its current state. The 2D representation and the assumption of in-plane strain and magnetic fields allow to reduce the CPU time but the physical concept of the present model can be implemented in the same manner in a 3D model. Simulations with 3D models will be helpful to get more detailed information, for example

on the role of boundary effects, which are likely to influence the threshold at which friction damping is activated. The model furthermore assumes a negligible convection effect, i.e. transport terms, for the magnetic quantities in the stationary vibration regime. This assumption can be verified in future studies as well as the effect of non-stationary electro-magnetic effects, such as eddy currents [19]. However, in its current state it has already provided useful information on the normal stress distribution and the evolution of the contact state

5. Conclusions and perspectives

In the present work, we introduce the concept of magnetofriction for vibration damping. In this concept, magnetic forces are used to generate the contact pressure while vibrations induce the tangential forces in the same contact interface.

The concept is demonstrated by the so-called Magnetofriction Sandwich Structure (MSS). The MSS comprises a core that consists of a permanently magnetized MagnetoActive Elastomer (MAE) and ferromagnetic steel skins. Due to the magnetic attraction forces between core and skins, the MSS can be assembled without glue or other additional mechanical means of fixation. Compared to other assembly strategies (e.g. use of bolts, screws, magnets), the flexible MAE in the core of the MSS adapts its shape to the deformations of the vibrating structure. This shape adaptability assures a distributed contact interface which enhances friction damping.

Random and harmonic vibrations are performed with the MSS to evaluate its amplitude-dependent characteristics. The backbones are identified into an original harmonic balance framework. The MSS shows a strongly nonlinear behavior for the first three modes. With increasing vibration magnitude, the natural frequency decreases, whereas the modal damping increases. This behavior is characteristic for friction damping. It is also shown that the Modal Strain Energy Fraction is very high compared to many other damping technologies. Moreover, the damping ratio is one of the highest obtained among all the studies dedicated to friction induced damping. It is remarkable that the best value has been obtained on the first eigenmode. The setup benefits from the fact that the contact pressure is low (about 2.4 kPa compared to 1 MPa for the ORION beam) and almost uniformly distributed over the entire domain.

A numerical model of the experiments is implemented for the study of the local contact state. The simulations show that the magnetic contact pressure is almost uniformly distributed in the contact interface which is favorable for friction damping. The comparison of normal and tangential forces in the contact interface confirms the dependence of the contact states on the vibration amplitude: from total stick for a small vibration magnitude to mainly sliding for high vibration magnitudes.

The present work can be classified as a proof of concept for magnetofriction. A topic for future works is the separation of the damping phenomena: viscoelastic damping, friction damping and eddy current damping. Another perspective for further inquisition lies in evaluating wear and damage over the entire life of the structure. The current sandwich is quite heavy because of the NeFeB particles. Instead of using a full H-MAE core, the core could be positioned where the structure deforms the most. The results of these studies will allow the design of magnetofriction devices with optimum dissipation capacities.

Acknowledgments

This work has been funded by the French company Moving Magnet Technologies SA and EIPHI Graduate School, ANR-17-EURE-0002.

6. CRediT authorship contribution statement

Svenja Hermann: Conceptualization, Investigation, Software, Validation, Writing – original draft, Visualization. Pauline Butaud: Writing – review & editing, Conceptualization. Rafael de O. Teloli: Data curation, Methodology. Jean-François Manceau: Writing – review & editing. Maxime Savary: Writing – review & editing, resources. Gaël Chevallier: Writing – review & editing, resources, Methodology, Supervision.

Declaration of conflicting interests

The authors declare no potential conflicts of interest with respect to the research, authorship, and/or publication of this article.

Appendix A. Experimental results for the two first vibration modes under harmonic excitation

Figures A.1 and A.2 depict the FRFs estimated for the second and third bending modes, respectively. The amplitude represents the ratio of the velocity measured on the structure and the acceleration measured on the base. Limiting frequencies for sliding and adhesion have been obtained by numerical modeling of the experiment for the to resonance modes. Even without recalibration of the model, the numerical results give a good approximation of the experimental limits for adhesion and sliding.

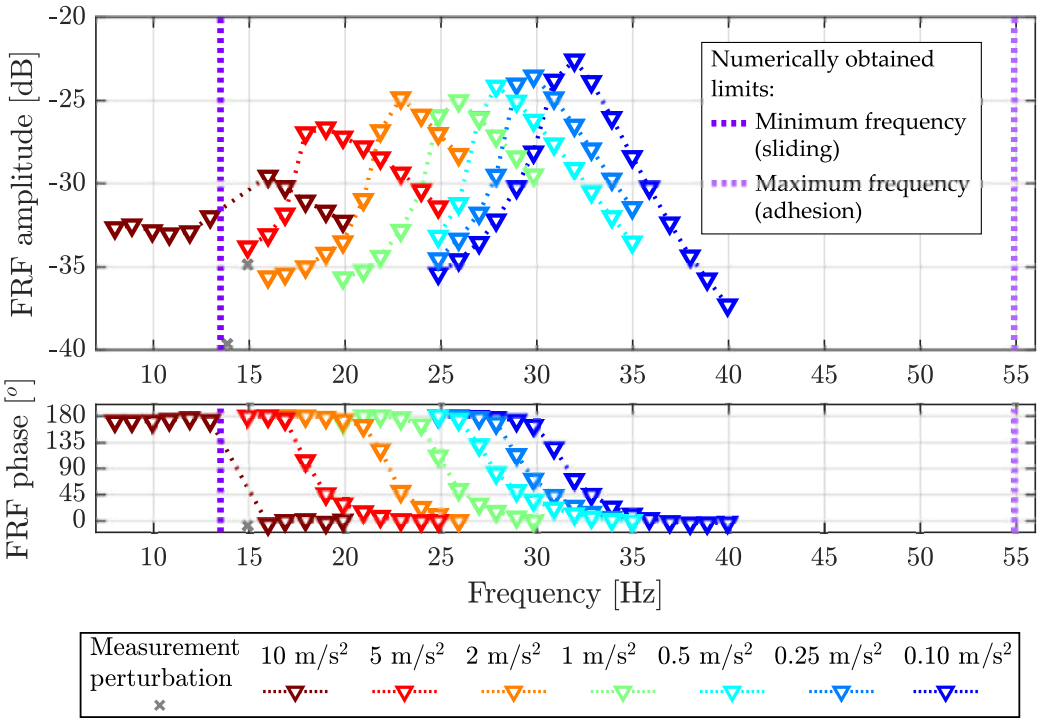

Figure A.1: Experimental results of harmonic vibration test for the first resonance mode: amplitudes and phases of the FRFs obtained for six different acceleration amplitudes with increasing -△- or decreasing -▽- frequency during the measurement.

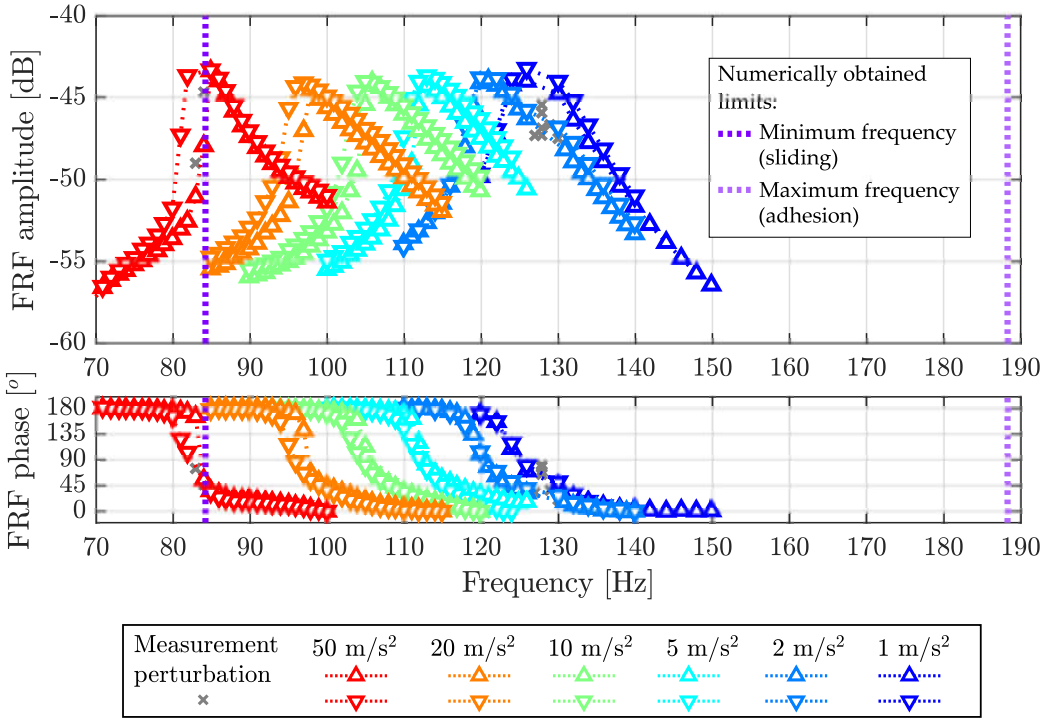

Figure A.2: Experimental results of harmonic vibration test for the second resonance mode: amplitudes and phases of the FRFs obtained for seven different acceleration amplitudes with decreasing -▽- frequency during the measurement.

Appendix B. Harmonic excitation and measurement of the Velocity fields

Fig. B.1 a shows the velocity fields of the deformed structure for three different acceleration magnitudes. The frequencies are chosen such as the resonance mode is excited for the corresponding acceleration magnitude. The velocity fields are normalized for each configuration with reference to the base (light green), hence the absolute values corresponding to the colors are not important for the comparison. The deformed configurations confirm, that the frequency range excites the third vibration mode as two regions with a strong displacements and three vibration nodes with the same velocity as the base are observed. Visual comparison of the three configurations shows no significant difference between the velocity fields.

In a second analysis, the velocity fields, measured for the different configurations, are compared point by point. For each configuration, the field contains N velocities measured on the different points j which, at the resonance, form an approximation of the k^{th} eigenvector $\boldsymbol{\Phi_k}$ as shown in Eq. ((B.1)), where the exponent $^{\mathrm{T}}$ indicates the transpose of the vector:

$$\boldsymbol{\Phi}_k = [v_1,\ v_2,\ \cdots,\ v_j,\ \cdots,\ v_N]^{\mathrm{T}}\ . \tag{B.1}$$

To compare the vectors between the three different configurations, the coefficients of a Modal Assurance Criterion (MAC) matrix are calculated by

$$MAC_{kl} = \frac{\boldsymbol{\Phi}_k^{\mathrm{T}} \cdot \boldsymbol{\Phi}_l}{||\boldsymbol{\Phi}_k||\,||\boldsymbol{\Phi}_l||^2} \qquad k,l = 1,2,3\ , \tag{B.2}$$

where k and l correspond to one of the three configurations. A coefficient MAC_{kl} of the matrix represents the correlation between velocity fields of the configuration k and l. If the coefficient is equal to 1, the eigenvectors are co-linear and that the velocity fields are identical. A coefficient equal to 0 means, that the eigenvectors are oriented in an orthogonal manner and that the velocity fields are very different. The 3x3 MAC matrix for the three tested configurations is shown in Fig. B.1 (b) in form of squares with size and color depending on the coefficient. The three values on the diagonal are equal to 1 since the velocity field of the three configurations are compared to themselves. The matrix shows, that there is a monotonic evolution of the mode shape with the excitation magnitude since the coefficients are different

from 1, but the variation is very small. In conclusion, it is stated that the nonlinearity does not affect the mode shape in a significant manner.

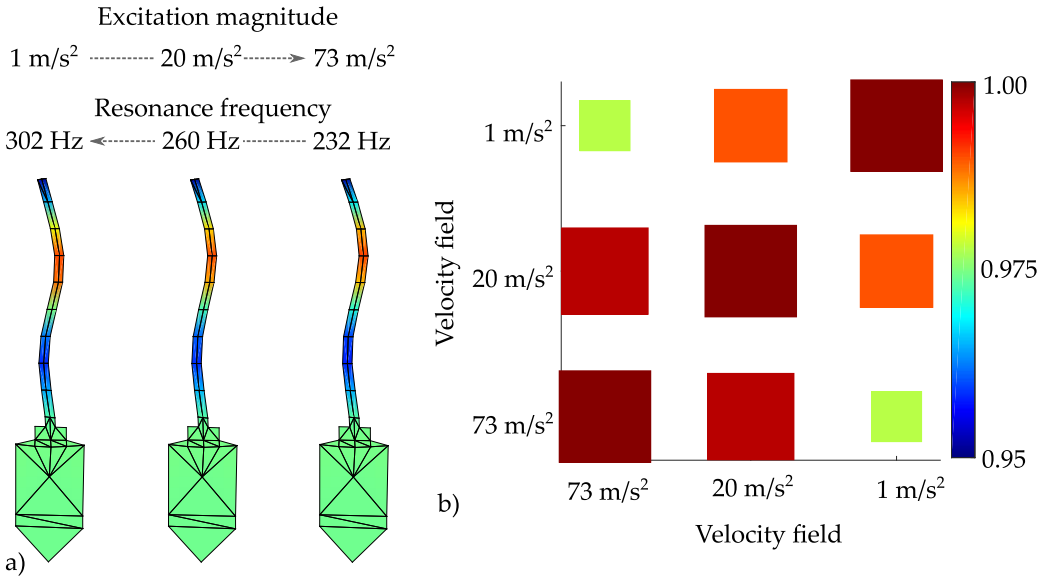

Figure B.1: Normalized mode shapes of the structure for the three excitation amplitudes (a) and modal assurance criterion (MAC) for the three configurations (b).

Appendix C. Results of the identification procedure

The figures below reveal the comparison of the FRFs measured experimentally and computed with the Harmonic Balance Method from the identification process described in section 3.4. The amplitude represents the ratio of the displacements measured on the structure and on the base [mm/mm].

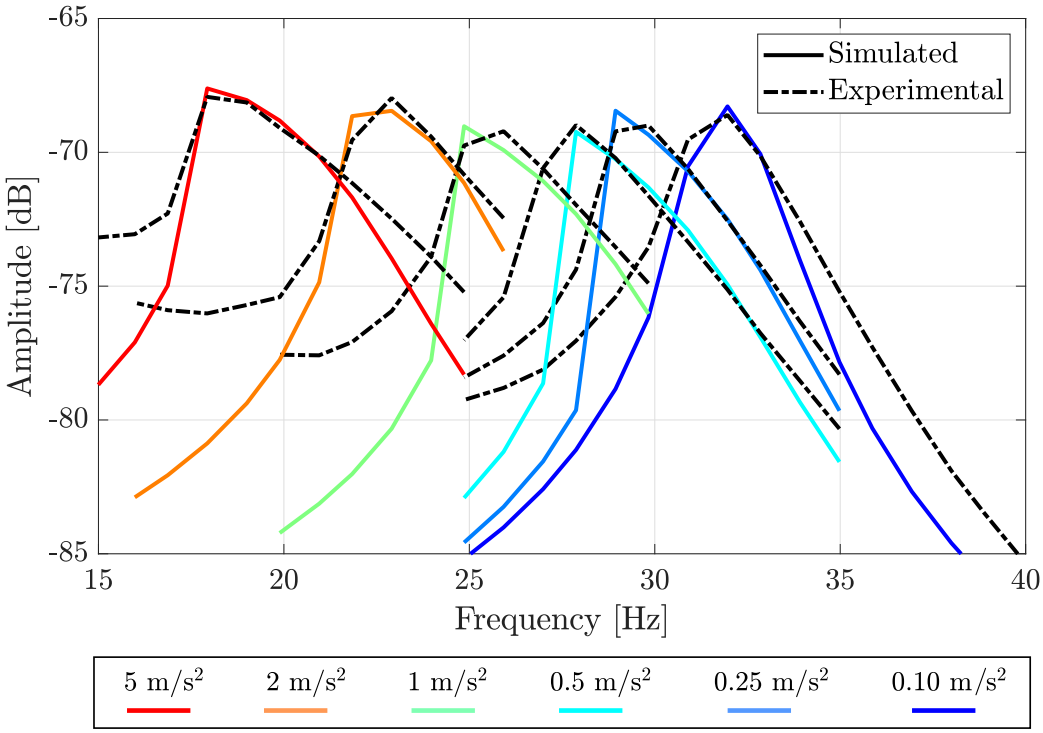

Figure C.1: Results of the identification process ("Simulated") for the harmonic vibrations of the first mode in comparison with experimental results.

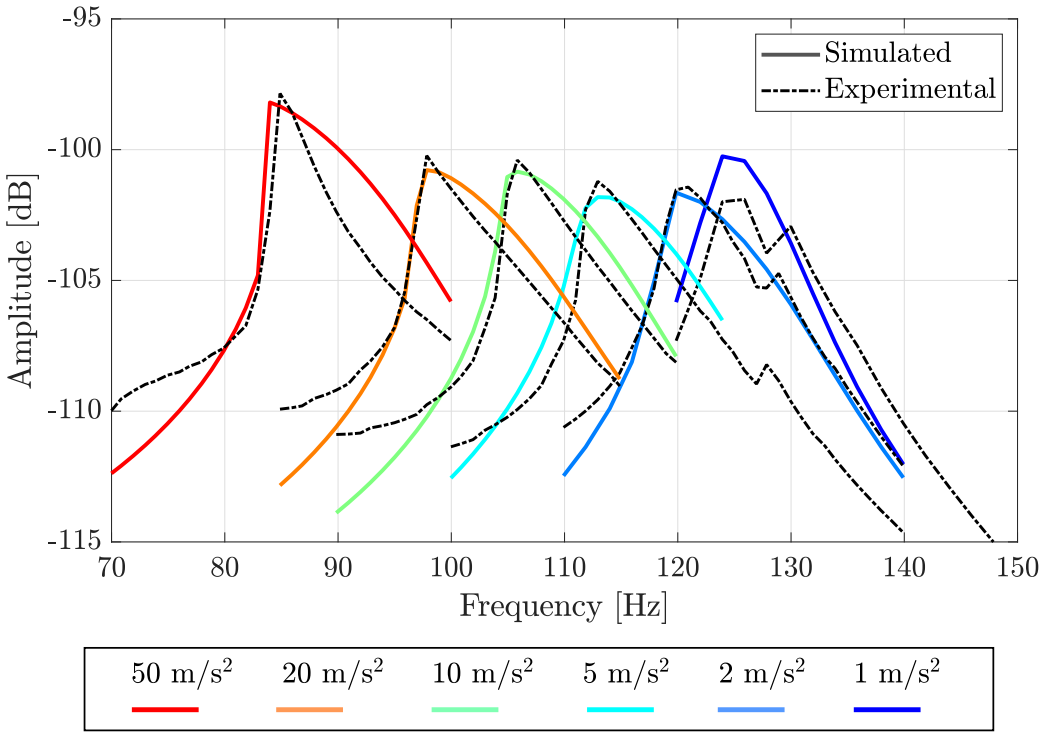

Figure C.2: Results of the identification process ("Simulated") for the harmonic vibrations of the second mode in comparison with experimental results.

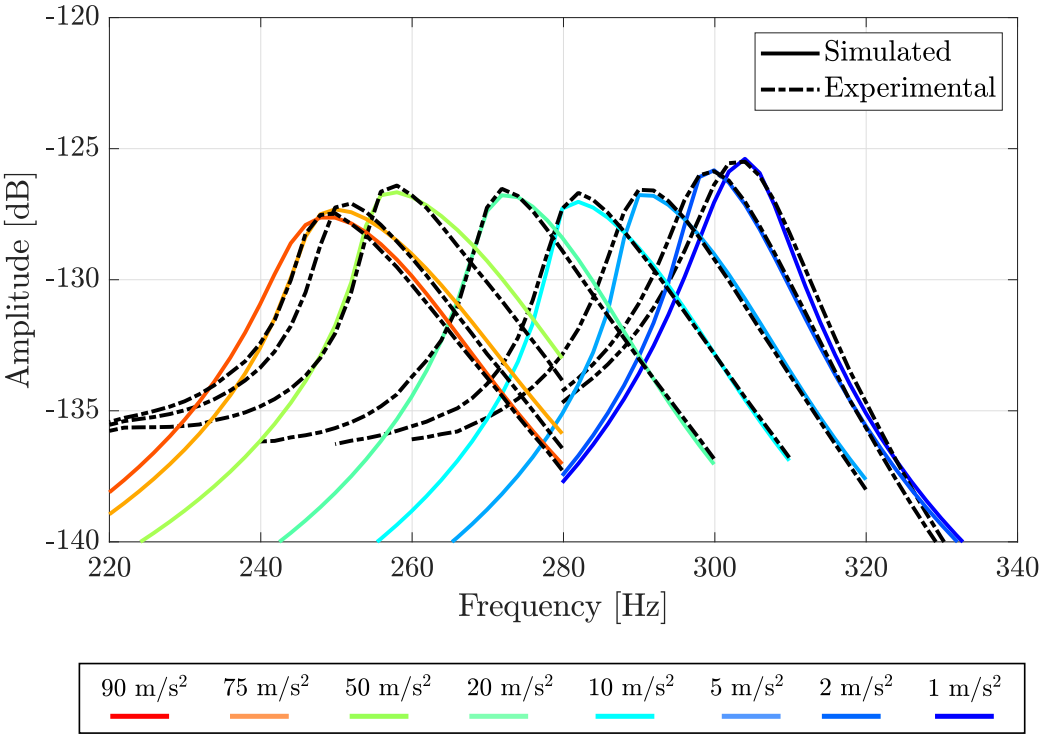

Figure C.3: Results of the identification process ("Simulated") for the harmonic vibrations of the third mode in comparison with experimental results.

Appendix D. Details on the models used to evaluate the local contact state (section 4)

Appendix D.1. Magneto-static equations

The magnetic flux density $\boldsymbol{B}$ is governed by the following equation:

$$div(\boldsymbol{B}) = 0 \,, \tag{D.1}$$

Moreover, the magnetic field $\boldsymbol{H}$ derives from the potential ψ^{mag}

$$\boldsymbol{H} = -\boldsymbol{grad}(\psi^{mag}) \,, \tag{D.2}$$

The constitutive behavior that links the magnetic flux $\boldsymbol{B}$ and the magnetic field $\boldsymbol{H}$ of the steel skin is governed by a non linear law (cf. figure D.1).

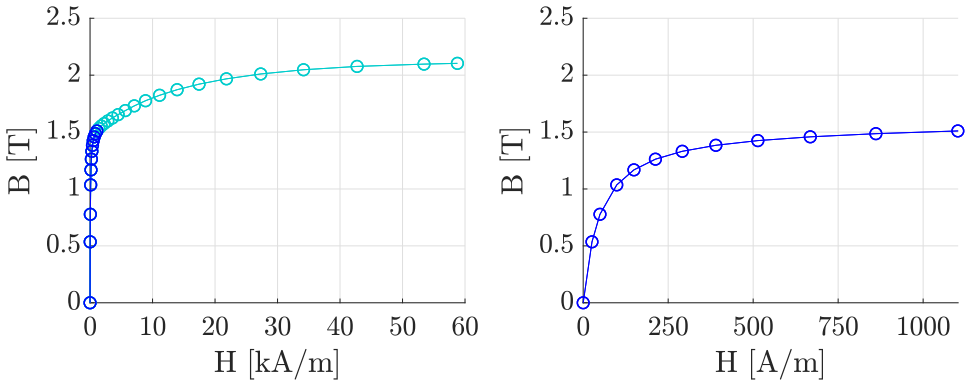

Figure D.1: Magnetization curve of the steel alloy M400-50A, represented in the full (a) and a restricted (b) measurement range.

Appendix D.2. Mechanical equations

The mechanical balance equations are implemented for stationary cases for which Cauchy's equation of motion is described by

$$\boldsymbol{div}\big(\boldsymbol{\sigma}\big) = \boldsymbol{0} \,, \tag{D.3}$$

where $\boldsymbol{\sigma}$ is the Cauchy stress tensor.

Appendix D.3. Prescribed displacement in the mechanical simulations

The prescribed displacement field is computed from the experimental data obtained with laser full field measurement and reported in Appendix C.

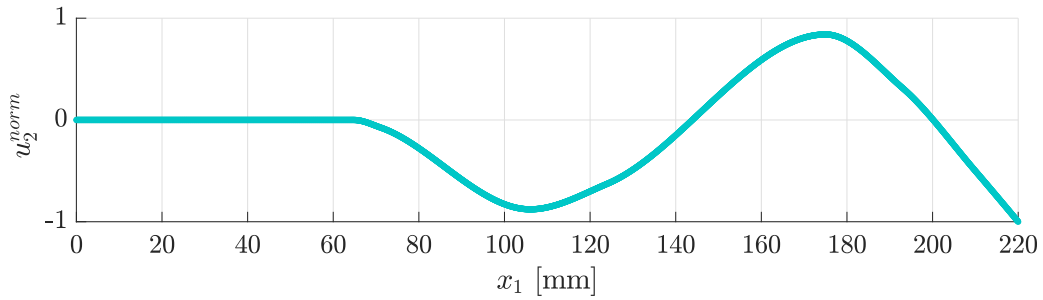

Figure D.2: Normalized modal displacement u_2^{norm}: displacement function obtained from interpolated experimental data $a = 1\,\mathrm{m/s^2}$.

Appendix E. Additional simulation results

Appendix E.1. Distribution of the magnetic flux density in the sample

The magnetization of the H-MAE patches generates a magnetic flux that propagates in the sandwich structure. The orientation and intensity of local magnetic flux density are represented in Fig. E.1 by the orientation and the color of the cones. The orientation of the residual flux density $\boldsymbol{B_r}$ of the patches is represented by red arrows in addition. The magnitude of the magnetic flux density is very high in the skins compared to the other parts and reaches 2.15 T at the maximum. The high magnetic permeability of the ferromagnetic material causes the flux to concentrate in the skins. The color gradient shows that the intensity of the flux density is not evenly distributed in the skins: the magnetic flux is concentrated at the intersection between two patches while the remaining section of the patch is only weakly magnetized (0.1 T on average). The weak magnetization is due to the material properties and the geometry of the patches, while the concentration at the intersection is caused by the magnetic circuit. At the intersection of two oppositely magnetized patches, closed loops of the magnetic flux form easily and the flux lines are dense.

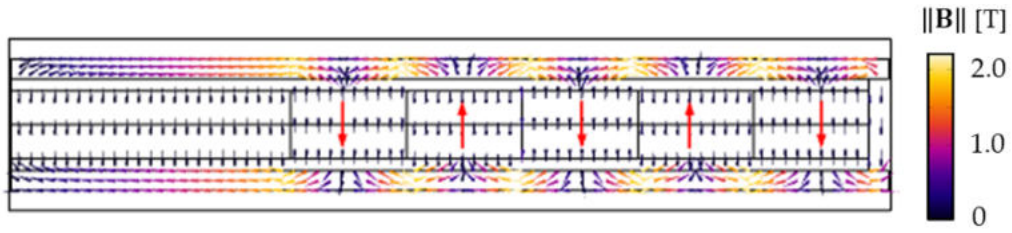

Figure E.1: Local magnetic flux density $\boldsymbol{B}$ in the sandwich structure (cones, color corresponding to magnitude $||\boldsymbol{B}||$) and orientation of the residual flux density $\boldsymbol{B_r}$ of the magnetic patches (red arrows).

Appendix E.2. Convergence study of the normal load

The contact pressure is governed by the computation of the magnetic forces. As mentioned in section 4, an artificial gap has been created as the conventional FE code is able to calculate the magnetically induced pressure only between magnetic and non-magnetic materials. The sensitivity analysis in Fig. E.2 shows that the local pressure decreases with the air-gap, which is comprehensible as the magnetic field decreases with the distance towards the magnetized MAE.

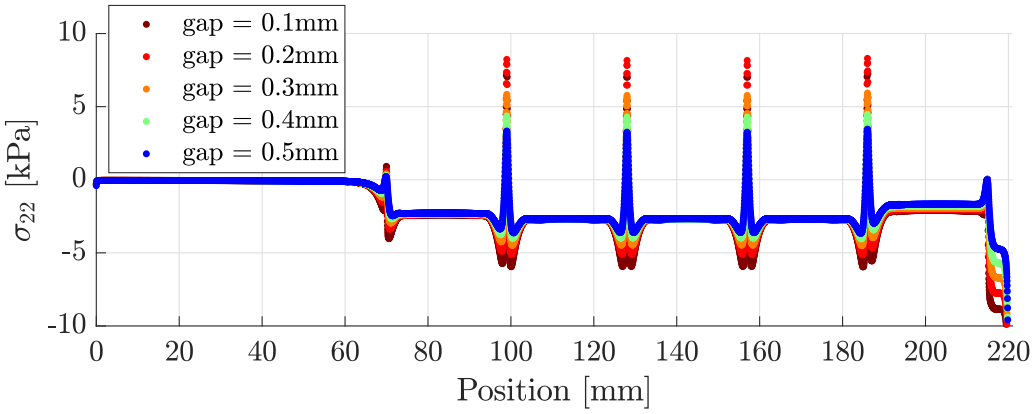

Figure E.2: Parametric study of the contact pressure as a function of the air gap.

The choice of 0.3mm was based on the pressure in the central regions of the five patches as the pressure peaks arise near singularity points of the geometry. The zoom on these regions in Fig. E.3 shows that the pressure decreases slightly stronger than before at distances above 0.3mm. The computation time, on the other hand, increased strongly with the reduction of the air gap

as the mesh becomes denser in the air gap and in adjacent regions. The choice of 0.3mm is a compromise between the calculation time accuracy of the force calculation.

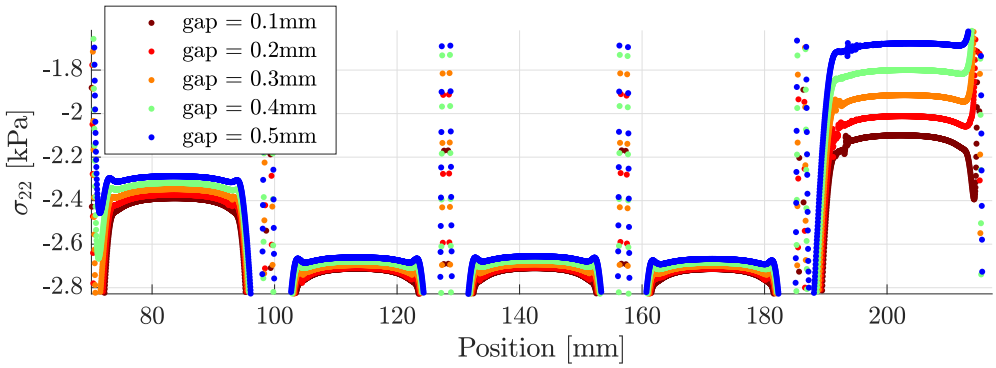

Figure E.3: Parametric study of the contact pressure as a function of the air gap - zoom on the regions where the patches are located.

Appendix F. Distribution of the glue points in the glued Magnetofriction Sandwich Structure (gMSS)

Figure F.1: Partly assembled gMSS in the sample holder prior to the positioning of the upper skin showing the glue points.

References

[1] P. Butaud, D. Renault, B. Verdin, M. Ouisse, G. Chevallier, In-core heat distribution control for adaptive damping and stiffness tuning of composite structures, Smart Materials and Structures 29 (6) (2020) 065002.

[2] G. Zhou, Q. Wang, Use of magnetorheological elastomer in an adaptive sandwich beam with conductive skins. part ii: Dynamic properties, International Journal of Solids and Structures 43 (17) (2006) 5403–5420.

[3] B. Nayak, S. Dwivedy, K. Murthy, Dynamic analysis of magnetorheological elastomer-based sandwich beam with conductive skins under various boundary conditions, Journal of Sound and Vibration 330 (9) (2011) 1837–1859.

[4] B. Nayak, S. Dwivedy, K. Murthy, Vibration analysis of a three-layer magnetorheological elastomer embedded sandwich beam with conductive skins using finite element method, Proceedings of the Institution of Mechanical Engineers, Part C: Journal of Mechanical Engineering Science 227 (4) (2013) 714–729.

[5] G. Hu, M. Guo, W. Li, H. Du, G. Alici, Experimental investigation of the vibration characteristics of a magnetorheological elastomer sandwich beam under non-homogeneous small magnetic fields, Smart Materials and Structures 20 (12) (2011) 127001.

[6] T. Szmidt, D. Pisarski, R. Konowrocki, S. Awietjan, A. Boczkowska, Adaptive damping of a double-beam structure based on magnetorheological elastomer, Shock and Vibration 2019 (2019) 16.

[7] B. Dyniewicz, J. Bajkowski, C. Bajer, Semi-active control of a sandwich beam partially filled with magnetorheological elastomer, Mechanical Systems and Signal Processing 60 (2015) 695–705.

[8] K. Popp, L. Panning, W. Sextro, Vibration damping by friction forces: theory and applications, Journal of Vibration and Control 9 (3–4) (2003) 419–448.

[9] M. Scheel, T. Weigele, M. Krack, Challenging an experimental nonlinear modal analysis method with a new strongly friction-damped structure, Journal of Sound and Vibration 485 (2020) 115580.

[10] N. Peyret, J.-L. Dion, G. Chevallier, P. Argoul, Micro-slip induced damping in planar contact under constant and uniform normal stress, International Journal of Applied Mechanics 2 (02) (2010) 281–304.

[11] H. Bouaziz, N. Peyret, M. Abbes, G. Chevallier, M. Haddar, Vibration reduction of an assembly by control of the tightening load, International Journal of Applied Mechanics 8 (06) (2016) 1650081.

[12] M. Vakilinejad, A. Grolet, O. Thomas, A comparison of robustness and performance of linear and nonlinear lanchester dampers, Nonlinear Dynamics (2020) 1–19.

[13] M. Brake, The mechanics of jointed structures: recent research and open challenges for developing predictive models for structural dynamics, Springer, 2017.

[14] R. de O. Teloli, P. Butaud, G. Chevallier, S. da Silva, Good practices for designing and experimental testing of dynamically excited jointed structures: The orion beam, Mechanical Systems and Signal Processing 163 (2022) 108172.

[15] N. Peyret, G. Chevallier, J.-L. Dion, Dynamic damping in joints: multiscale model taking into account defects in a nominally plane surface, International Journal of Applied Mechanics 8 (08) (2016) 1650097.

[16] M. Brake, C. Schwingshackl, P. Reuß, Observations of variability and repeatability in jointed structures, Mechanical Systems and Signal Processing 129 (2019) 282–307.

[17] H. Dai, Z. Huang, W. Wang, A new permanent magnetic friction damper device for passive energy dissipation, Smart Materials and Structures 23 (10) (2014) 105016.

[18] E. Choi, G. Choi, H. T. Kim, H. Youn, Smart damper using the combination of magnetic friction and pre-compressed rubber springs, Journal of Sound and Vibration 351 (2015) 68–89.

[19] M. Amjadian, A. Agrawal, Modeling, design, and testing of a proof-of-concept prototype damper with friction and eddy current damping effects, Journal of Sound and Vibration 413 (2018) 225–249.

[20] M. Amjadian, A. Agrawal, Planar arrangement of permanent magnets in design of a magneto-solid damper by finite element method, Journal of Intelligent Material Systems and Structures 31 (7) (2020) 998–1014.

[21] S. Hermann, P. Butaud, G. Chevallier, J.-F. Manceau, C. Espanet, Magnetic and dynamic mechanical properties of a highly coercive mre based on ndfeb particles and a stiff matrix, Smart Materials and Structures 29 (2020) 105009.

[22] M. Berthillier, C. Dupont, R. Mondal, J. J. Barrau, Blades forced response analysis with friction dampers, Transactions of the ASME 120 (1998) 468–474.

[23] S. Ye, K. A. Williams, Torsional friction damper optimization, Journal of Sound and Vibration 294 (3) (2006) 529–546.

[24] T. Caughey, Equivalent linearization techniques, The Journal of the Acoustical Society of America 35 (11) (1963) 1706–1711.

[25] N. Peyret, J.-L. Dion, G. Chevallier, A framework for backbone experimental tracking: Piezoelectric actuators, stop-sine signal and kalman filtering, Mechanical Systems and Signal Processing 78 (2016) 28–42.

[26] R. M. Lacayo, M. Allen, Updating structural models containing nonlinear iwan joints using quasi-static modal analysis, Mechanical Systems and Signal Processing 118 (2019) 133–157.

[27] G. Chevallier, S. Ghorbel, A. Benjeddou, Piezoceramic shunted damping concept: testing, modelling and correlation, Mechanics & Industry 10 (5) (2009) 397–411.

[28] C. Hammami, E. Balmes, M. Guskov, Numerical design and test on an assembled structure of a bolted joint with viscoelastic damping, Mechanical Systems and Signal Processing 70 (2016) 714–724.

[29] G. Chevallier, S. Ghorbel, A. Benjeddou, A benchmark for free vibration and effective coupling of thick piezoelectric smart structures, Smart Materials and Structures 17 (6) (2008) 065007.

[30] L. Hirsinger, N. Daher, Les tenseurs de contraintes électromagnétiques [electromagnetic stress tensors], AFM, Maison de la Mécanique, 39/41 rue Louis Blanc, 92400 Courbevoie, France (FR) (2013).

[31] D. Ivaneyko, V. Toshchevikov, M. Saphiannikova, G. Heinrich, Mechanical properties of magneto-sensitive elastomers: unification of the continuum-mechanics and microscopic theoretical approaches, Soft Matter 10 (13) (2014) 2213–2225.

[32] M. Jolly, J. Carlson, B. Muñoz, T. Bullions, The magnetoviscoelastic response of elastomer composites consisting of ferrous particles embedded in a polymer matrix, Journal of Intelligent Material Systems and Structures 7 (6) (1996) 613–622.

[33] K. Danas, S. Kankanala, N. Triantafyllidis, Experiments and modeling of iron-particle-filled magnetorheological elastomers, Journal of the Mechanics and Physics of Solids 60 (1) (2012) 120–138.

[34] E. Galipeau, P. Castañeda, The effect of particle shape and distribution on the macroscopic behavior of magnetoelastic composites, International Journal of Solids and Structures 49 (1) (2012) 1–17.

[35] P. Castañeda, E. Galipeau, Homogenization-based constitutive models for magnetorheological elastomers at finite strain, Journal of the Mechanics and Physics of Solids 59 (2) (2011) 194–215.

[36] F. P. Bowden, F. P. Bowden, D. Tabor, The friction and lubrication of solids, Vol. 1, Oxford university press, 2001.